ACS OMEGA

http://pubs.acs.org/journal/acsodf

Article

Ultrasound-Triggered Microbubbles: Novel Targeted Core–Shell for the Treatment of Myocardial Infarction Disease

Aliyeh Ghamkhari, Hossein Ahmadi Tafti, Shahram Rabbani, Marjan Ghorbani, Mohammad Adel Ghiass, Fariborz Akbarzadeh, and Farhang Abbasi*

Cite This: *ACS Omega* 2023, 8, 11335–11350

Read Online

ACCESS | Metrics & More | Article Recommendations | Supporting Information

ABSTRACT: Myocardial infarction (MI) is known as a main cardiovascular disease that leads to extensive cell death by destroying vasculature in the affected cardiac muscle. The development of ultrasound-mediated microbubble destruction has inspired extensive interest in myocardial infarction therapeutics, targeted delivery of drugs, and biomedical imaging. In this work, we describe a novel therapeutic ultrasound system for the targeted delivery of biocompatible microstructures containing basic fibroblast growth factor (bFGF) to the MI region. The microspheres were fabricated using poly(lactic-*co*-glycolic acid)-heparin-polyethylene glycol- cyclic arginine-glycine-aspartate-platelet (PLGA-HP-PEG-cRGD-platelet). The micrometer-sized core–shell particles consisting of a perfluorohexane (PFH)-core and a PLGA-HP-PEG-cRGD-platelet-shell were prepared using microfluidics. These particles responded adequately to ultrasound irradiation by triggering the vaporization and phase transition of PFH from liquid to gas in order to achieve microbubbles. Ultrasound imaging, encapsulation efficiency cytotoxicity, and cellular uptake of bFGF-MSs were evaluated using human umbilical vein endothelial cells (HUVECs) *in vitro*. *In vivo* imaging demonstrated effective accumulation of platelet- microspheres injected into the ischemic myocardium region. The results revealed the potential use of bFGF-loaded microbubbles as a noninvasive and effective carrier for MI therapy.

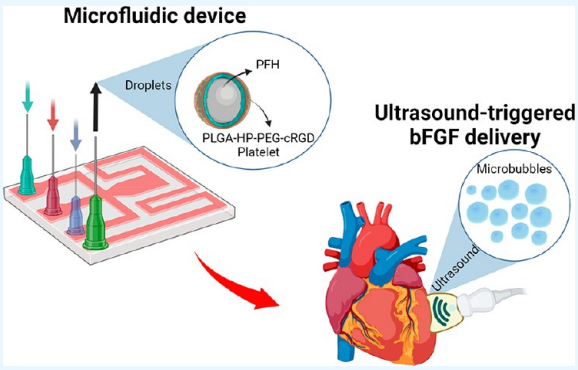

1. INTRODUCTION

Cardiovascular diseases have been known as the first cause of death and a serious threat to human health.[1,2] Myocardial infarction (MI) is a common cardiovascular disease consisting of the irreversible death (necrosis) of heart muscle due to lack of oxygen. The MI undergoes progressive conditions and usually leads to myocardial fibrosis, diastolic function, and even weakened ventricular contraction, heart failure (HF), malignant arrhythmia, and sudden death.[3]

Previous studies have demonstrated that angiogenesis-related active growth factors, such as basic fibroblast growth factor (bFGF),[4,5] vascular endothelial growth factor (VEGF),[6,7] and hepatocyte growth factor (HGF),[8] could induce blood vessel formation, reduce pro-inflammatory signals,[9] promote renal repair in acute kidney injury,[10] reduce structural and functional damage,[11] and help the migration of endothelial cells in the infarcted area.

Systemic drug delivery has diminished efficacy because of slow tissue penetration, short *in vivo* half-life, and the tendency to cause systemic side effects.[12] However, studies have shown that bFGF direct injection into the heart has many risks which limit its clinical applications.[13] In addition, the bFGF delivery system should maximize the biological activity of bFGF as well as minimize the impact on systemic tissues. To overcome these limitations, we introduce the bFGF delivery using heparin conjugated due to high binding affinities and the biological activity increase.[14,15]

Recently, microbubbles (MBs) as ultrasound (UTS) contrast agents have been explored as a promising drug delivery system in clinics.[16,17] In addition, ultrasound-targeted microbubbles can improve intracellular delivery of the bioactive materials due to the response of the microbubbles to physical effects such as acoustic fluid streaming, cavitation, pressure variation, and local hyperthermia.[18,19]

MBs are core–shell particles in which a gas core is covered by a shell.[20−22] MBs have a diameter of less than 6 μm.[23] The shell is made of surfactants, lipids,[24] liposomes,[25] albumin,[26] protein,[27] and biocompatible and biodegradable polymers like poly(lactic-*co*-glycolic acid) (PLGA),[28,29] poly(vinyl alcohol) (PVA),[30] chitosan,[31] and alginate.[32]

Received: January 4, 2023
Accepted: February 7, 2023
Published: March 14, 2023

Scheme 1. Schematic Diagram of the Chemical Formula of the PLGA-HP-PEG-cRGD (a) and the Process of the PLGA-HP-PEG-cRGD-platelet-PFH MBs Formation (b)

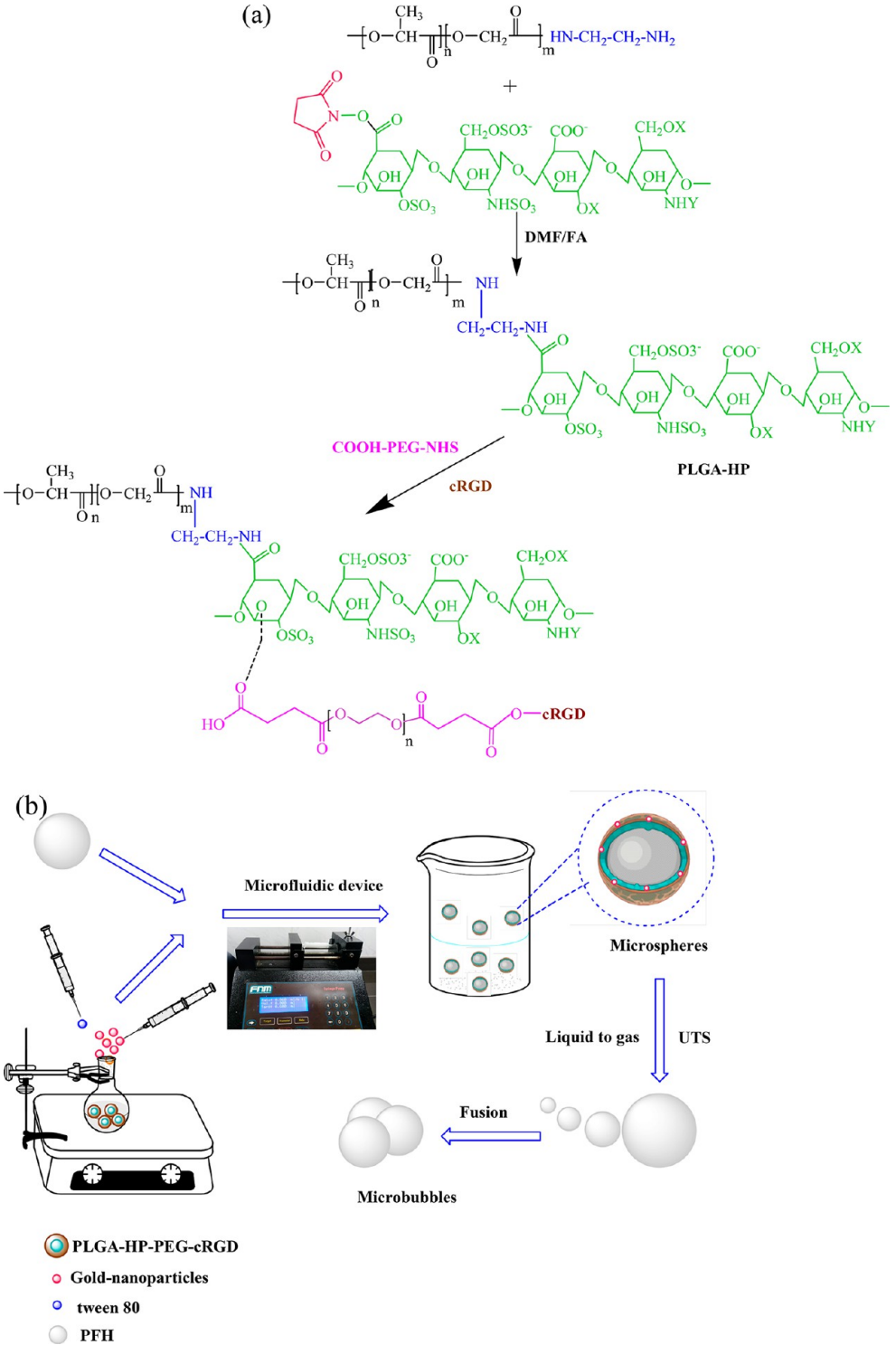

The gas core includes an insoluble and dense gas such as air,[33] perfluorocarbon,[34] and sulfur hexafluoride.[35] Perfluorocarbons (PFCs), as chemically and biologically inert materials, can be used for intravascular circulation.[34] The low stability of perfluoropropane (PFP) droplets causes them to be converted into foam in blood circulation before reaching the target region; it is difficult to control their droplet-to-microbubble transition.[36] In order to obtain nanodroplets with higher stability, perfluorohexane (PFH) was used in this work. PFH has a boiling point of about 58−60 °C.[36]

Phase-change contrast agents, as a novel ultrasound-mediated modality, can vaporize and be converted into microbubbles under the action of ultrasound.[37] Liquid PFH has a "liquid-to-gas" phase transition (PT) and can be converted into a gas via a nonthermal mechanism termed acoustic droplet vaporization (ADV), which is called the

https://doi.org/10.1021/acsomega.3c00067
ACS Omega 2023, 8, 11335−11350

cavitation effect.[38] The drugs encapsulated into PFH droplets are released under ultrasound irradiation. Therefore, PFH, due to its favorable properties, has been selected for biomedical applications such as ultrasound imaging and therapy.[39,40] In addition, the high solubility of oxygen and *in vivo* stability of PFH provide high potential for US imaging via liquid-to-gas transition.[38]

A series of biological effects, such as cavitation and sonoporation, is created in the process of the phase transition, which has the potential to treat cardiovascular diseases and tumors.[41] Afterward, ultrasound-responsive polymer/PFH nanodroplets have effectively been applied by drugs loaded for on-demand drug delivery.[36] In ischemic myocardium-targeted probe (IMTP)-Fe_3O_4−PFH nanoparticles (NPs), PFH plays a role due to ADV triggered by ultrasound, thereby allowing PFH-coated NPs to enhance US imaging.[42]

An important goal of advanced drug delivery is to controllably supply drugs to specific sites in the body, which often requires using carrier vehicles that efficiently encapsulate.[43] The loaded drugs are systemically transferred using targeting ligands to the objective site, thus reducing the amount of drugs needed.[44] Platelets were used as targeting ligands, play a crucial role in developing vascular inflammation, and contribute importantly to reperfusion injury. The platelet is correlated with the location of necrotic or ischemic areas.[45,46] There are glycoprotein (GP) IIb/IIIa receptors on the surface of activated platelets.[47,48] The arginine-glycine-aspartate (RGD) peptide can bind to GP IIb/IIIa receptors. Cyclic RGD (cRGD) has demonstrated greater affinity than linear RGD, resulting in more stability for binding to the GP IIb/IIIa receptor.[49,50]

In this study, we present a novel formulation of ultrasound-triggered phase transition microspheres (MSs) synthesized by a microfluidic technique. The PFH (core)/PLGA-HP-PEG-cRGD (shell) MSs were prepared with uniform sizes and loading capacities of more than 90%. The liquid PFH was vaporized via acoustic droplet vaporization. The subsequent microbubbles of the phase-change microspheres (PCMSs) were generated via UTS irradiation and temperature. Finally, bFGF-MSs were prepared and evaluated as theranostic agents in MI diseases.

2. EXPERIMENTAL SECTION

2.1. Materials. Poly(D,L-lactide-*co*-glycolide) (PLGA) [molecular weight (MW) = 25,000 g mol^{-1}; lactic acid:glycolic acid = 75:25, with acid end groups (PLGA-COOH)], 1-ethyl-3-(3-(dimethylamino)propyl)carbodiimide (EDC) (98.0%), *N*-hydroxysuccinimide (NHS) (98%), ethylenediamine (EDA), polyethylene glycol (HO-PEG-OH) with MW = 4,000 g mol^{-1}, poly(vinyl alcohol) (PVA), fluorescein-5-isothiocyanate (FITC), hydrogen tetrachloroaurate (III) trihydrate ($HAuCl_4 \cdot 3H_2O$) (99.5%), fetal bovine serum (FBS), dicyclohexylcarbodiimide (DCC) (99%), 4-(dimethylamino)pyridine (DMAP) (99%), and succinic anhydride (98%) were purchased from Sigma-Aldrich. Tween 80, formamide (FA), and *N*,*N*-dimethylformamide (DMF) (98%) were purchased from Merck. Heparin (HP) sodium salt (≥180 IU/mg, from pork intestine mucosa) was purchased from Carl Roth GmbH. Cyclic arginine-glycine-aspartate (cRGD) was purchased from GL-Biochem Ltd. (Shanghai, China). Perfluorohexane (PFH) was purchased from Alfa-Aesar. Basic fibroblast growth factor (bFGF) was purchased from Royan Institute, Iran. Chitosan (degree of deacetylation = 75−85%) was purchased from Pelican Biotech & Chemical (India).

2.2. Synthesis of PLGA-NHS. To synthesize PLGA-NHS, PLGA-COOH (500 mg, 0.02 mmol), EDC (35 mg, 0.18 mmol), and NHS (19 mg, 0.125 mmol) were dissolved in anhydrous methylene chloride (10 mL) and stirred at room temperature for 24 h under nitrogen atmosphere. The final product was precipitated with cold diethyl ether (5 mL) and dried under a vacuum to remove the solvent.

2.3. Synthesis of PLGA-monoamine-Terminated (PLGA-NH_2). In the second step, PLGA-NHS (500 mg, 0.2 mmol) and 60 μL of EDA were dissolved in CH_2Cl_2 (15 mL) by stirring at room temperature for 24 h. Then the mixture was dialyzed against distilled water for 3 days at room temperature and finally lyophilized to obtain the product.

2.4. Synthesis of PLGA-HP. PLGA-HP was synthesized according to the NHS/EDC method.[51] Specifically, the reaction was done between the carboxyl group of activated heparin and the amine group of PLGA and led to amide bond formation. For this purpose, low molecular weight heparin salt (250 mg, 0.02 mmol), NHS (32 mg, 0.27 mmol), and EDC (10 mg, 0.05 mmol) were dissolved in DMF/FA (5 mL) for 4 h at 4 °C. After the PLGA-NH_2 (100 mg, 0.004 mmol) was reacted according to Scheme 1(a) with the above mixture by stirring for 24 h at room temperature, the product was dialyzed against distilled water for 3 days at room temperature and then lyophilized to obtain the product.

2.5. Synthesis of COOH-PEG-NHS. For this purpose, first a mixture containing HO-PEG-OH (50 mg, 0.01 mmol), succinic anhydride (25 mg, 0.02 mmol), and DMAP (5 mg, 0.04 mmol) was dissolved in dichloromethane (CH_2Cl_2) solution and stirred for 24 h at 25 °C. Then the solvent was evaporated using a rotary evaporator and the product was purified via recrystallization in isopropyl alcohol. The final product was collected with vacuum filtration. Then the HOOC-PEG-COOH, EDC, and NHS (0.3:0.06:1.5 molar ratio) were dissolved in anhydrous CH_2Cl_2 (10 mL) by stirring at room temperature for 24 h under nitrogen atmosphere to activate the carboxylic groups of PEG. The product was precipitated with cold diethyl ether (30 mL) and dried under vacuum to remove the solvent.

2.6. Synthesis of PLGA-HP-PEG-cRGD. PLGA-HP-conjugated HOOC-PEG-NHS was obtained by a direct coupling reaction via DMAP/DCC chemistry.[52] First, PLGA-HP (200 mg, 0.005 mmol) and HOOC-PEG-NHS (50 mg, 0.01 mmol) were dissolved in the mixture of DMF/FA (10 mL) solvent. Then DMAP and DCC were added to the solution under a nitrogen atmosphere. After the reaction was mixed for 24 h, the reaction mixture was precipitated in cold diethyl ether. After filtering, the product was dried in a vacuum to eliminate the solvent. The solution of PLGA-HP-PEG-NHS in anhydrous DMF/FA was poured dropwise into the cRGD solution. After continuous stirring for 48 h, the resultant solution was dialyzed against distilled water for 3 days at room temperature to remove the unreacted mixture. The conjugate PLGA-HP-PEG-cRGD was then lyophilized (Scheme 1(a)).

2.7. Synthesis of Chitosan-Wrapped Gold Nanoparticles. In a typical preparation, an aqueous solution of $HAuCl_4$ (100 μL) was mixed with an aqueous stock solution of chitosan as a protecting agent (1%) (3 mL). The solution was heated to 70 °C, and while stirring at this temperature for approximately 2 h, the reaction solution turned red color

https://doi.org/10.1021/acsomega.3c00067
ACS Omega 2023, 8, 11335−11350

immediately, indicating the formation of gold nanoparticles. The solution was then cooled to room temperature.

2.8. Isolation of Platelets. Platelets were separated from whole sheep blood by differential centrifugation. The plasma blood bag was poured into a 50 mL falcon and centrifuged for 5 min at 600 rpm to remove RBC. Then, platelet-rich plasma (PRP) was prepared by adding it into a 2 mL microtube and centrifuging for 15 min at 3200 rpm. The platelets were resuspended in PBS using an anticoagulant and ACD, and collected for subsequent experiments.

2.9. Instrumentation. Fourier transform infrared (FT-IR) spectra of the samples were obtained using a Shimadzu 8101 M FT-IR (Shimadzu, Kyoto, Japan) at a wavenumber range of 4000−400 cm^{-1}. Proton nuclear magnetic resonance (^{1}HNMR) spectra were obtained at 25 °C using an NMR (400 mHz) Bruker spectrometer (Bruker, Ettlingen, Germany). The samples were prepared in deuterated chloroform and dimethyl sulfoxide solvents (DMSO-d_6). Ultraviolet−visible (UV−vis) spectra were taken on a Shimadzu 1650 PC UV−vis spectrophotometer (Shimadzu, Kyoto, Japan). The morphology of the MBs was studied by a Zeiss-EM10C-100 kV transmission electron microscope (TEM, Germany) and optical microscopy. The zeta potential, size distribution, average diameter, and polydispersity index (PDI) of the MSs were measured with a Malvern Nano ZS90 Zetasizer (Malvern Instruments, UK) at 25 °C. The employed ultrasound devices (UTS) were a device working at an acoustic frequency of 1.7 MHz and an acoustic intensity of 1−600 mW cm^{-2} (Sahand University Technology, Tabriz, Iran) and another device working at an acoustic frequency of 1.5 MHz and an acoustic intensity of 35 mW cm^{-2} (Exogen Ultrasound). The field emission scanning electron microscopy (FE-SEM) was carried out using a MIRA3 microscope (TESCAN, Czech) to determine the morphology of the cells and MSs.

2.10. Preparation of Microspheres. 100 mg of PLGA-HP-PEG-cRGD was dissolved in DMSO and dialyzed against deionized (DI) water. 300 μL of PLGA-HP-PEG-cRGD water solution and 300 μL of gold nanoparticles were ultrasonicated for 30 min. Then, two drops of Tween 80 were added to the mixture and stirred for 15 min. The obtained solution and perfluorohexane were injected using two independent syringe pumps at a predetermined constant flow rate. The obtained microspheres from the microfluidic device were stabilized in a 1% PVA solution and collected (Scheme 1(b)).

2.11. Preparation of bFGF-loaded PLGA-HP-PEG-cRGD and *In Vitro* Release Study. PLGA-HP-PEG-cRGD (50 mg) and bFGF (50 μg) were suspended in 2 mL of PBS at 4 °C in a rotating condition for 48 h. bFGF-loaded PLGA-HP-PEG-cRGD was collected by centrifugation and washed with PBS to remove free bFGF. Then bFGF-loaded PLGA-HP-PEG-cRGD was prepared as microspheres (bFGF-MSs) and suspended in 2 mL of PBS containing 1 mg/mL bovine serum albumin at 37 °C with and without ultrasound irradiation. After predetermined times, the supernatants were collected, and the amount of the released bFGF was measured using an enzyme-linked immunosorption assay (ELISA kit, according to the manufacturer's instruction). The encapsulation efficiency (EE) of the MSs was calculated by eq 1.

$$\mathrm{EE}\ (\%) = \frac{\mathrm{bFGFtotal} - \mathrm{bFGFsuper}}{\mathrm{bFGFtotal}} \times 100 \quad (1)$$

2.12. *In Vitro* Cytotoxicity Study. The cytotoxic effects of bFGF-MSs and free bFGF were evaluated by the MTT assay. The HUVECs were cultured in RPMI-1640 medium, including 1% penicillin and 10% FBS in culture dishes with 5% CO_2, and seeded at a density of 1.3×10^5 cells per well. The incubated cells were followed by treatment with different concentrations (0, 10, 50, 100, 200 μg/mL) of blank bFGF-platelet MSs for 24 and 48 h. Afterward, 50 μL of MTT solution (2 mg/mL) was poured into each well and again incubated for 4 h. Then the media was transferred and exchanged with 100 μL of DMSO and incubated for 30 min. Finally, the optical absorbance was evaluated at 570 nm using a microplate reader (Elx808, Bio Tek, USA).

2.13. Fluorescent Labeling of bFGF with Fluorescein Isothiocyanate. The bFGF solution, bFGF-MSs, and bFGF-platelet MSs were labeled with fluorescein isothiocyanate (FITC) in order to investigate the bFGF distribution in *in vitro* experiments. For this purpose, 1 mL of FITC solution (100 μg/mL in DMSO) was poured slowly into bFGF-MSs and bFGF-platelet MSs. The mixture was stirred for 4 h at 25 °C in darkness. The labeled bFGF (FITC-bFGF), FITC-bFGF-MSs, and FITC-bFGF-platelet-MSs were dialyzed in order to eliminate the unconjugated FITC. Then the FITC-bFGF, FITC-FITC-bFGF MSs, and FITC-bFGF-platelet-MSs solutions were lyophilized.

2.14. Fluorescence Imaging *In Vitro*. HUVECs were cultured and underwent different treatments, including FITC-bFGF, FITC-bFGF MSs, and FITC-bFGF-platelet MSs solution containing 10% FBS. UTS was generated by an acoustic frequency of 1.0 MHz and an acoustic intensity of 270 mW cm^{-2}. Treated HUVECs were exposed to ultrasound irradiation, as reported previously.[53] The ultrasound transducer was placed in a water tank at 37 °C and a spongy rubber ultrasound shield was applied to focus ultrasound on the bottom of the cell plate. Then the cells were incubated and imaged with a Nikon fluorescence microscope (Nikon ECLIPSE 80i, Ruikezhongyi Company, Beijing, China).

2.15. Flow Cytometry. The effect sof using MB on FITC-bFGF, FITC-bFGF MSs, and FITC-bFGF-platelet MSs uptake were traced by flow cytometry using HUVECs. The cells were cultured and exposed to the different treatments, including bFGF only, FITC-bFGF, FITC-bFGF MSs, and FITC-bFGF-platelet MSs groups using ultrasound irradiation (+UTS) and without ultrasound irradiation (−UTS), respectively. The blank control served as untreated HUVECs. The treated cells were trypsinized and washed with cold PBS, and resuspended for flow cytometry. Control, bFGF only, FITC-bFGF, FITC-bFGF MSs, and FITC-bFGF-platelet MSs were studied in the flow cytometer.

2.16. *In Vitro* Targeting. HUVECs were seeded in culture dishes at a density of 1×10^4 cells per dish. After 24 h, the cells were allocated into two groups: targeted and nontargeted MSs. Both groups were incubated with 100 μL of FITC-bFGF MSs and FITC-bFGF-platelet MSs for 3 h, washed with PBS, and fixed with 4% paraformaldehyde for 10 min. Afterward, the dishes were washed with PBS three times and protected from light for FESEM (without FITC) and florescent microscope (with FITC) analyses.

2.17. Ethics Statement. The working protocol was carried out by the National Institutes of Health guide for the care and use of the Laboratory (NIH Publications No. 8023, revised 1978).

2.18. *In Vivo* Targeting Ability. To study the targeting efficiency of the MSs, two model rats were randomly selected and shaved. The *in vivo* fluorescence imaging of the rat hearts

https://doi.org/10.1021/acsomega.3c00067
ACS Omega 2023, 8, 11335−11350

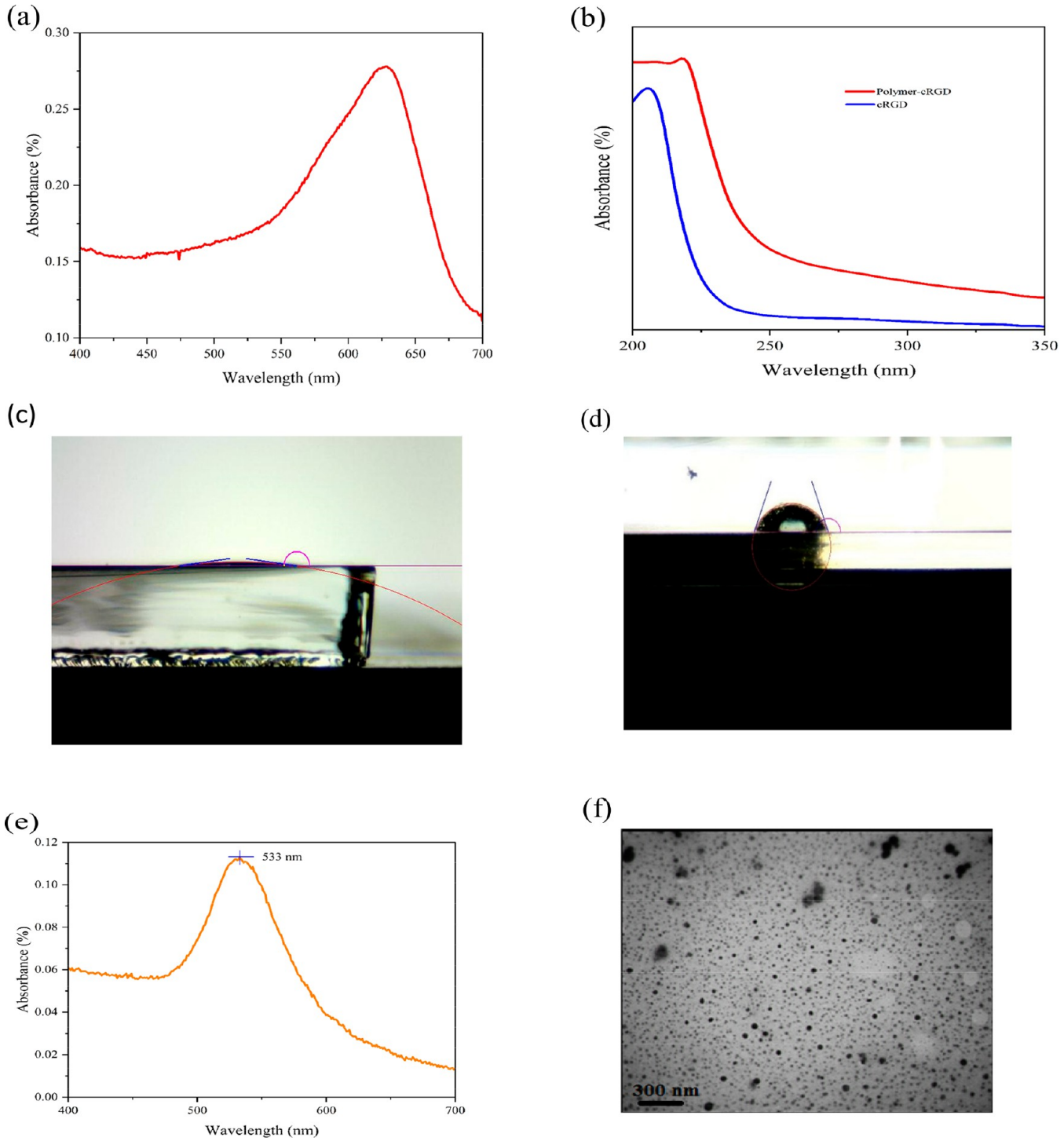

Figure 1. UV−vis spectra of PLGA-HP solution at 632 nm (a) and PLGA-HP-PEG-cRGD and cRGD solutions (b), hydrophobic/hydrophilic nature of the PLGA and PLGA-HP evaluated by water contact angle (WCA) measurements (c, d), UV−vis spectrum of chitosan-stabilized gold nanoparticles (e), and TEM image of chitosan-stabilized gold nanoparticles (f).

was performed at the Preclinical Core Facility (TPCF) based at Tehran University of Medical Sciences, at 1 min exposure time. The excitation and emission filters were set to 470 and 535 nm, respectively. In the preliminary exploration, the model of myocardial ischemia in rats was induced. Afterward, 100 μL of the FITC-bFGF MSs and FITC-bFGF-platelet MSs was injected via the tail vein immediately and photographed after 2 h without ultrasound.

3. RESULTS AND DISCUSSION

We chose PLGA, HP, and HOOC-PEG-COOH as the polymer system due to their well-confirmed biocompatible properties and safety in clinical use. PLGA is an FDA-approved biodegradable and biocompatible polymer.[54] In this work, PEGylation was used to provide a spacer in order to preserve the sufficient distance between the polymer and the MB surface. The destruction of microbubbles with ultrasound was

https://doi.org/10.1021/acsomega.3c00067
ACS Omega 2023, 8, 11335−11350

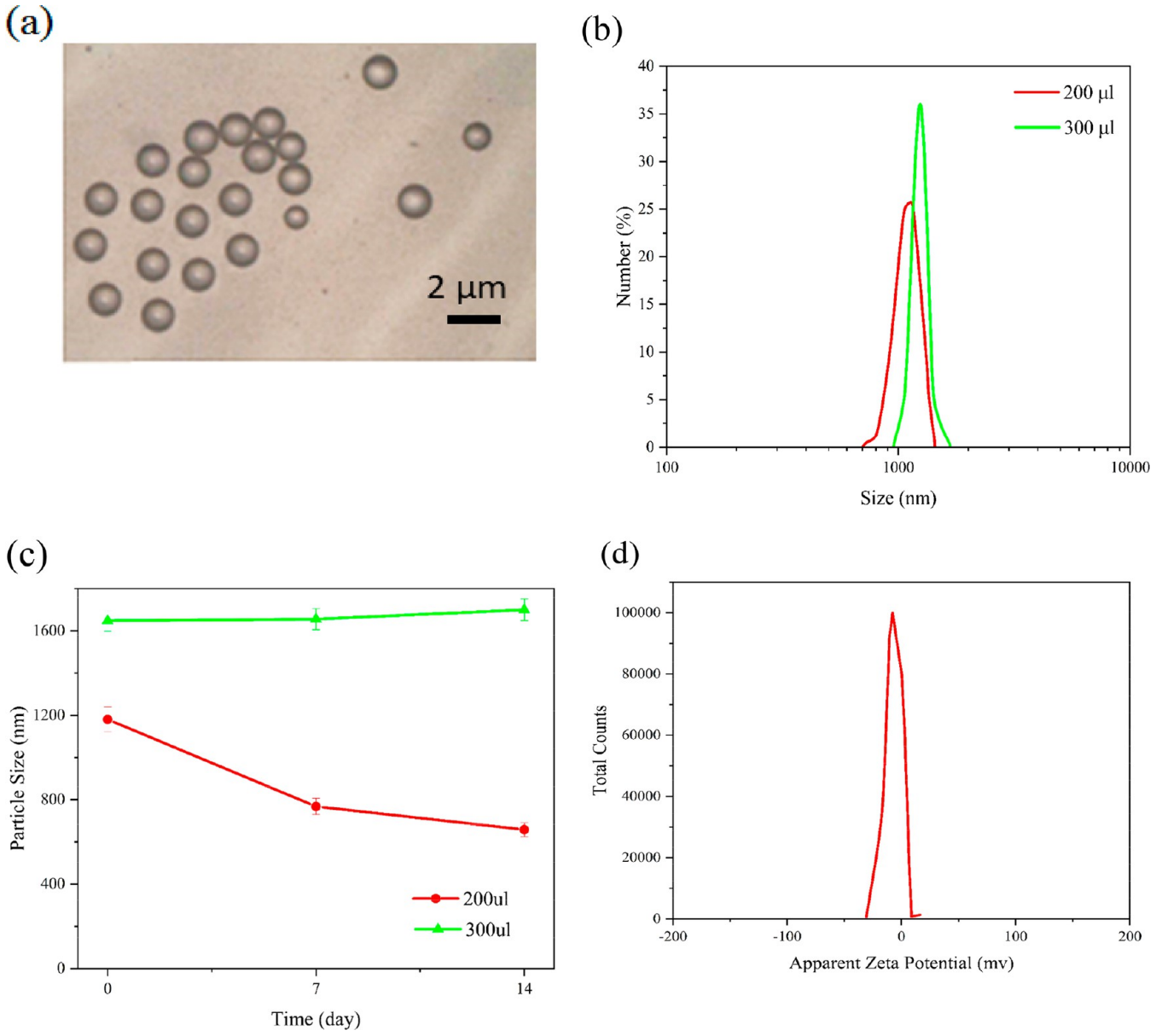

Figure 2. Optical microscopy images (a) and average particle size measured by Zetasizer (b, c) of the MSs at flow rates of 1 μL/min PFH and 250 μL/min for the composition of polymer solution with 300 and 200 μL gold nanoparticles on days 0, 7, and 14 (c), and the zeta potential of microspheres with 300 μL of gold nanoparticles (d).

assayed as an excellent strategy to improve their permeability and promote the specific delivery of therapeutics.[55]

3.1. Characterizing the Synthesized Materials. The FTIR spectra of the PLGA-NHS, PLGA-NH_2, PLGA-HP, and PLGA-HP-PEG-cRGD are demonstrated in Figure S1. The FTIR spectrum of PLGA-NHS contains the following peaks: C−O−C stretching vibration at 1288 cm^{-1}, the stretching vibration of the C−O group at 1353 cm^{-1}, and aliphatic C−H stretching vibration at 2897 cm^{-1}. Conjugation of EDA to PLGA-NHS was confirmed by FTIR spectroscopy, in which a new absorption band of the amide bond in PLGA-NH_2 appeared at 1678 cm^{-1}.

To confirm the conjugation of heparin to PLGA-NH_2, the absorption bands at 1241 cm^{-1} (S═O asymmetric stretching) and 1653 cm^{-1} (C═O asymmetric stretching) are the two prominent characteristic peaks of the heparin. However, some changes in the sulfate and carboxylate absorption bands appeared when HP was conjugated to PLGA. The characteristic absorption band (S═O asymmetric stretching) shifted to 1264 cm^{-1} in the conjugated heparin. In addition, the formation of amide bonds between the carboxyl and amine groups of EDA was confirmed by the absorption band appearing at 1683 cm^{-1}. In addition, PLGA-HP was characterized by a new peak at 1757 cm^{-1}, which was related to the carbonyl stretching vibration of the PLGA-HP complex, and the peak detected at 3300−3600 cm^{-1} can be related to the hydroxyl group of conjugated heparin. The FTIR spectra of the PLGA-HP-PEG sample are indicated in Figure S1. The FTIR spectrum of the PLGA-HP-PEG displays absorption bands of hydroxyl groups at 3435 cm^{-1}, C═O group stretching vibration at 1733 cm^{-1}, and the C−O−C stretching vibration at 1100 cm^{-1} (Figure S1).

The successful syntheses of PLGA-NHS, PLGA-NH_2, and PLGA-HP-PEG-NHS were further confirmed employing

https://doi.org/10.1021/acsomega.3c00067
ACS Omega 2023, 8, 11335−11350

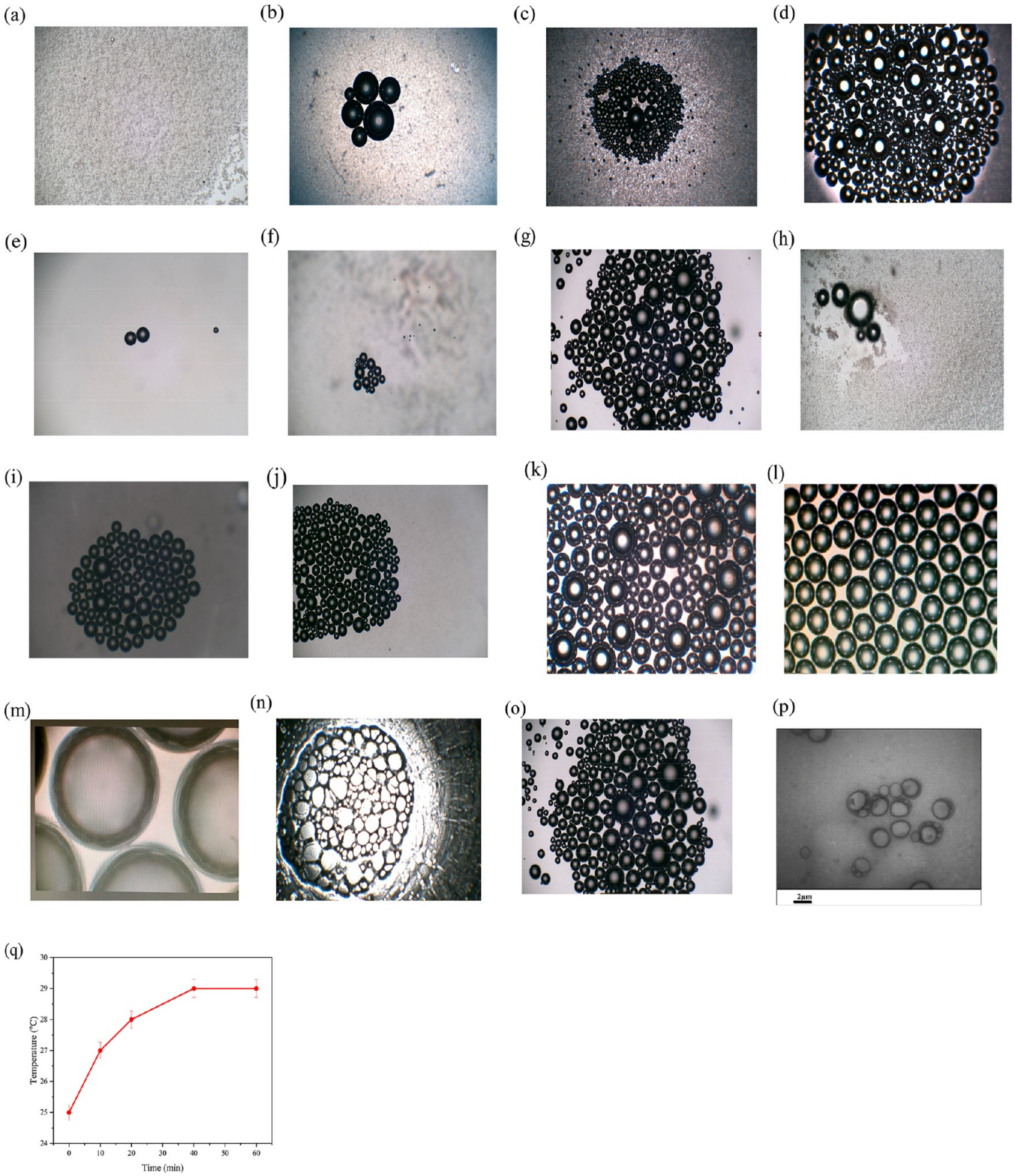

Figure 3. Light-microscopy images of microbubbles at different temperatures (58−60 °C (a), 65 °C (b), 75 °C (c), 90 °C (d)), under ultrasound irradiation at 35 mW/cm^2 for 10 min (e), 20 min (f), and 80 min (g), under ultrasound irradiation at 270 mW/cm^2 for 5 min (h) and 15 min (i), and under ultrasound irradiation at 330 mW/cm^2 for 7 min (j) and 12 min (k). Light-microscopy images of monodispersed microbubbles (l), core−shell microbubbles observed with a thin layer of polymer on the surface (m), dried microbubbles (n), the two drops of water added to the dried microbubbles (o), TEM image of the microbubbles (p) and the time course of the temperature change (q).

^{1}HNMR spectroscopy, as demonstrated in Figure S2. The ^{1}HNMR spectrum of the PLGA-NHS shows chemical shifts at 1.4 ppm (d), and 1.59 ppm (a) associated with (CO-C$\underline{H}_2$-C$\underline{H}_2$-CO) and (O-CH(C$\underline{H}_3$)-CO). The chemical shifts at 4.69 (c) and 5.2 ppm (b) were attributed to (OC-C$\underline{H}_2$O) and (OC-C$\underline{H}$O (CH$_3$)) (Figure S2A). The ^{1}H NMR spectrum of

https://doi.org/10.1021/acsomega.3c00067
ACS Omega 2023, 8, 11335−11350

PLGA-NH_2 showed chemical shifts at 1.5 (a), 4.78 (b), and 5.25 (c) ppm related to the methyl and methylene protons of the PLGA backbone. The chemical shift at 2.2 ppm (f) is related to the NH_2 protons. The chemical shift at 3.47 and 4.3 ppm (d, e) is related to the methylene protons of NH-CH_2-CH_2-NH_2, (Figure S2B). The PLGA-HP-PEG copolymer was successfully synthesized using the synthetic route demonstrated in Scheme 1(a) using DCC/DMAP chemistry. The ^{1}H NMR spectrum of the final product displayed successful synthesis of PLGA-HP-PEG copolymer in which the main signals related to PLGA moiety (a), (b), (c) at 1.46, 4.8, and 5.2 ppm of the lactide units in PLGA. The chemical shifts at 3.38 and 4.1 ppm (d, e) are related to the NH-CH_2-CH_2-NH, respectively. Also, the chemical shifts at 2.1 (f), 3.1, and 3.5 (g, h) ppm were attributed to CH-NH of heparin and PEG moiety (methylene hydrogen of the PEG), respectively (Figure S2C).

The conjugated heparin to PLGA was evaluated using toluidine blue.[56] For this purpose, 3 mL of the toluidine blue solution (0.005%), dissolved in NaCl (0.9%), was added to 1 mL of solution (6 μg/mL) PLGA-HP copolymer and stirred for 2 h at 37 °C. Then, 2 mL of hexane was added to the above mixture and shaken for 30 s to separate the heparin dye complex. Afterward, the absorbance of this solution was measured at 632 nm using UV−vis (Figure 1a). The relationship between concentration and absorbance was obtained by a standard curve. The content of conjugated heparin to PLGA-HP was calculated 65%.

The results obtained from FTIR, HNMR, and toluidine blue analyses demonstrate that HP is successfully conjugated to PLGA. Heparin, due to its high negative charge density,[14] easily binds to many proteins like bFGF and provides a controlled release of bFGF.[15] Such a strong affinity to HP is helpful in protecting bFGF from chemical inactivation and proteolytic degradation and increases bFGF bioactivity and stabilization.[14,15]

The PLGA-HP-PEG-cRGD and cRGD were successfully synthesized and confirmed by UV−vis spectrum (Figure 1b). cRGD indicates an absorption peak at 205 nm, and PLGA-HP-PEG-cRGD showed the same absorption at about 220 nm.

The hydrophobic/hydrophilic nature of the PLGA and PLGA-HP was estimated by water contact angle (WCA) measurements. The PLGA, as a hydrophobic material, had a water contact angle of 70.3°, which significantly decreased by the conjugation of HP to 7.2° due to the hydrophilicity of heparin (Figure 1c,d).

Chitosan is a linear polysaccharide and has a number of possible biomedical applications. The presence of abundant hydroxyl and amino groups in chitosan enhances its reducing, chelating, and stabilizing characteristics.[57] Therefore, chitosan can be applied as an effective stabilizing and reducing agent for preparing gold nanoparticles.[58] In the present work, citric acid was used to dissolve chitosan, and the gold nanoparticles were synthesized using chitosan as a protecting agent through electrostatic attraction between positively charged amino groups in chitosan chains and negatively charged particles.[58] The gold nanoparticles were monodispersed compared to citrate-stabilized gold nanoparticles.[59]

Hence, a green and facile method was employed at 70 °C compared to the other methods. The formed gold nanoparticles were pale red in color and demonstrated the absorption peak at 533 nm (Figure 1e). From the TEM image (Figure 1f), the gold nanoparticles were spherical and almost monodispersed, with the average particle size being around 25 nm.

3.2. Characterizing Prepared MSs and MBs. In this work, the core−shell MSs were prepared using a simple microfluidic device as well as an oil/water emulsion method. The designed microfluidic device allowed to control of the flow rates of two different solutions by employing two independent syringe pumps. The inner solution was a perfluorocarbon, PFH, with a boiling point at about 60 °C and a vapor pressure of 27 kPa. PFH was used to prevent the coalescence of the particles and enhance the particle stability. The outer aqueous phase was the polymeric solution containing PLGA-HP-PEG-cRGD/gold nanoparticles/Tween 80 mixture. MSs were made by using a designed microfluidic. The final MSs were collected in the PVA (1%) solution as a stabilizing agent. The MSs were prepared in the microfluidic at the constant flow rate of 1 μL/min for PFH and varying flow rates of 200, 250, 300, 350, 400, and 450 μL/min for polymer solution. According to the optical microscopy results (Figure 2a), the prepared MSs were nearly monodispersed, and the particle size of the MSs prepared at the flow rate of 250 μL/min with two different gold nanoparticle concentrations were evaluated on days 0, 7, and 14 by the Zetasizer (Figure 2b,c). The average particle sizes of the prepared core−shell microspheres after three different periods (0, 7, and 14 days) were about 1648, 1656, 1700 and 1181, 658, 768 nm for 300 and 200 μL of gold nanoparticles, respectively. The initial stability tests demonstrated that the concentration of gold nanoparticles and polymer in the original suspension affected the stability of the MSs. Figure 2c displays how the diameter varied with time for samples of 1181 to 1648 nm prepared using gold nanoparticle suspensions. Therefore, the PFH-MSs led to stable MSs with an equal amount of gold nanoparticles and polymer in the original suspension.

The surface charge of the MSs was measured using zeta potential analysis by a Zeta plus analyzer, and the surface charge of the prepared negatively charged MSs was about −7.11 mV (Figure 2d).

The temperature responsiveness of the MSs was evaluated by the bright field microscopic observation. Although the vaporization temperature of PFH was 59−60 °C, the MSs did not exhibit any change at 58−60 °C (Figure 3a). Interestingly, when the temperature rose to 65 °C, liquid PFH cores underwent phase-change; a small amount of the MSs started to form MBs (Figure 3b) and the bubbles amount and their volumes increased at 75 °C (Figure 3c). When the temperature reached 90 °C, more MSs were converted into enlarged MBs (Figure 3d). However, fewer MBs were observed at 90 °C because some of the formed MBs started to be destroyed; after 15 min at this temperature, almost all the MBs were destroyed.

PFH-MSs are interesting for ultrasound-triggered delivery systems. To disrupt the PFH-loaded MSs, they were exposed to ultrasound (UTS) (with an acoustic frequency of 1.5 MHz and an acoustic intensity of 35 mW cm^{-2}) for 10−80 min. When the MSs were exposed to ultrasound, the variations of the formed MBs were observed via light microscopy (Figure 3e−g). The volume of the MBs increased to about 2 μm from their original size, which can be attributed to the increasing number of vaporized MSs and more MBs formed at 80 min (Figure 3g). In addition, it was found that the MBs had a relatively gentle slope of size enhancement and would not explode immediately after the ultrasound. As shown in Figure 3, the smallest microbubbles were seen at around 10 min, and the largest microbubbles were seen at around 80 min. They

https://doi.org/10.1021/acsomega.3c00067
ACS Omega 2023, 8, 11335−11350

completely lost their spherical structure at about 100 min. Also, the formed MBs were investigated with another ultrasound system at the acoustic frequency of 1.7 MHz and the acoustic intensity of 270 mW cm^{-2} for 5 and 15 min (Figure 3h,i) and the acoustic intensity of 330 mW cm^{-2} for 7 and 12 min (Figure 3j,k). Approximately 40% of the MSs were converted into MBs at 7 min after ultrasound irradiation. Also, the formation rate of MBs was increased during 12 min at 330 mW cm^{-2}. However, due to the high boiling point of PFH (58 °C), MSs can be more easily vaporized by low acoustic intensity.[37,38] As mentioned before, gold nanoparticles were used for the preparation of stable MSs in this work. On the other hand, gold nanoparticles were able to reduce the UTS pressure threshold in ADV and, in combination with UTS irradiation, can increase the attenuation coefficient of the UTS waves in the medium, act as a nucleation point for cavitation bubble formation, absorb energy leading to hyperthermia, decrease the cavitation threshold, and generate free radicals.[60] Therefore, the preparation of microbubbles has been done with low acoustic intensity.

Light-microscopy images demonstrated monodispersed MBs (Figure 3l), and MBs were observed with a thin layer of polymer on the surface (Figure 3m). After complete evaporation and drying of the MSs (Figure 3n), a few MS of distilled water was poured, and the reformation of microbubbles was observed (Figure 3o). A TEM image of the MBs showed their spherical morphology with a polymeric portion as the shell around them (Figure 3p). The size of the microbubbles was measured before their bursting; their diameters were about 1815 nm on average after 10 min of ultrasound irradiation. It was seen that with the acoustic MS vaporization the temperature was enhanced to approximately 30 °C (Figure 3q), indicating a lower thermal impact created by ultrasound due to the low intensity, which is an ideal feature for a selected treatment. Therefore, unlike the temperature-responsiveness, which can hurt the adjacent tissue, this slight increase in temperature would be safe. UTS, as the most appropriate technique, has been applied to convert MSs into microbubbles. This threshold-based technique provides a temporal trigger point for the improved control of the therapeutic process.[61] The volume of the MBs was enhanced to the micrometer scale from their original size. The number of vaporized MSs was increasing, and we found that the MSs would not burst quickly after expanding to a certain size. This procedure was relatively slow, and after some minutes, the loosening of their structure was observed. At this point, MBs would penetrate the objective tissue for targeting ability and improving the effect.[45]

Scheme 2 represents the three-step process of the formation of bFGF-platelet MSs. Exploiting ultrasound at the MI site, the liquid PFH core in the MSs vaporized and converted the MSs into microbubbles; MI therapy was carried out by UTS-triggered bFGF delivery.

3.3. Ultrasound Imaging *In Vitro*. The traditional MBs can significantly increase the echo signals, and their large particle sizes could restrict their application to imaging in the blood pool. A "small-to-big" phase-transformation protocol can solve this issue of the traditional MBs and pass through the blood pools; the targeted MBs could penetrate the intended tissues due to their initially small particle sizes.[45,62]

To demonstrate whether the phase transition of the MSs was excited by ultrasound irradiation *in vitro*, we investigated the duration of ultrasound irradiation at the frequency of 2.5 MHz.

Scheme 2. Schematic Representation of the Three-Step Process of Formation of bFGF-platelet MSs[a]

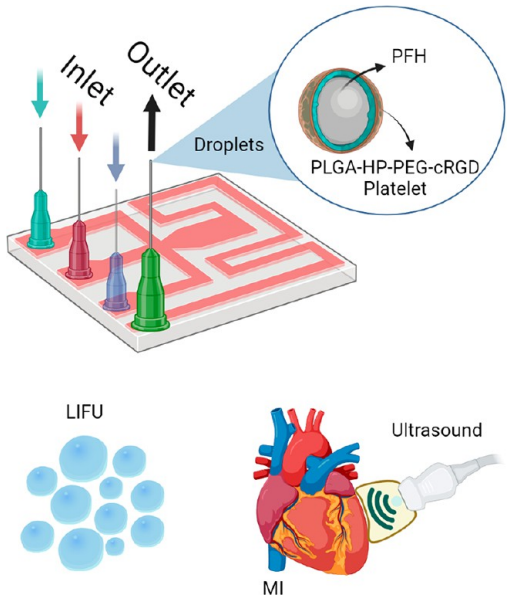

[a]With ultrasound assistance at the MI site, the liquid PFH core in the MSs vaporized and converted the MSs into microbubbles for the subsequent MI therapy by UTS-triggered bFGF delivery.

Figure 4 shows that enhanced signals of microbubbles were generated after the US irradiation under the brightness (B) mode. A minimal amount of MBs was formed with a duration of 2 and 5 min, declaring that the power did not have adequate ability to trigger the phase transformation because of the stiffness of the polymer shell at this time. The large amount peaked at 20−30 min and then began to decrease at 30 min. These results exhibited that the bFGF-MSs could convert into MBs triggered via ultrasound irradiation, the power of which provided lengthened time. Although multiple MBs were created via an ultrasound system with a higher frequency during the short time, the created MBs were collapsed quickly due to the higher frequency than the MBs formed at lengthened times.[63]

3.4. *In Vitro* Cytotoxicity Study and bFGF Release from MBs. The high encapsulation (98%) of bFGF indicated that the MSs, as appropriate vehicles, were able to efficiently encapsulate bFGF. The release behavior of bFGF from the MSs was evaluated in the PBS solution at 37 °C with and without US irradiation. The accumulative release of bFGF from MBS is displayed in Figure 5. After 150 h, the accumulative concentration of the released bFGF was 17.4 pg/mL without ultrasound and 1840 pg/mL with ultrasound, indicating that with ultrasound irradiation, the concentration of the released bFGF was higher than the case without ultrasound irradiation. Moreover, the bFGF release was increased due to the ADV effect and ultrasound responsiveness, and the diffusion of the bFGF was enhanced into the surrounding medium of the MBs.

To demonstrate whether the bFGF-MSs can be efficiently biosafe and biocompatible before and after loading bFGF, we incubated the MSs with HUVECs to evaluate the cytotoxicity and assess the cellular distribution. As shown in Figure 6a, the proliferation profiles of HUVECs during incubation with MSs were examined for 24 and 48 h. The MSs demonstrated excellent cell viability against HUVECs with increasing the

https://doi.org/10.1021/acsomega.3c00067
ACS Omega 2023, 8, 11335−11350

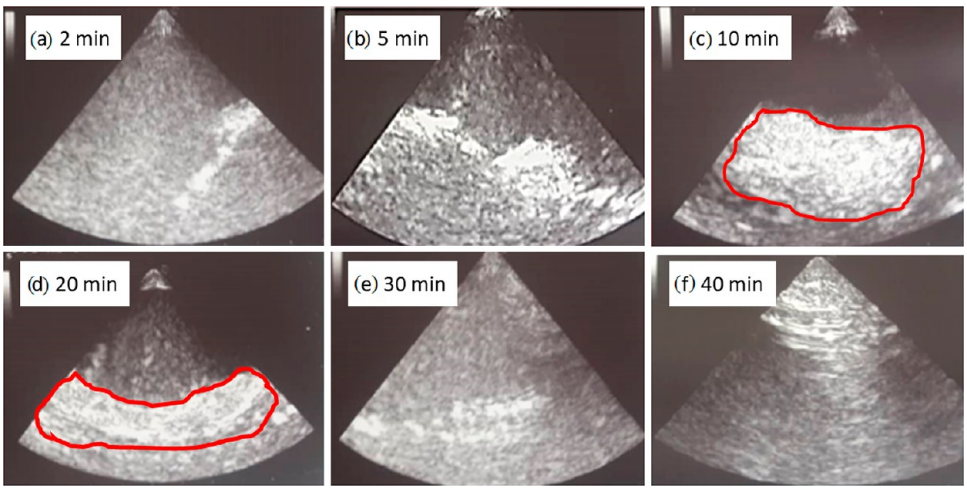

Figure 4. Quantitative echo-signal intensity of MSs on B-mode corresponding to UTS images at different times.

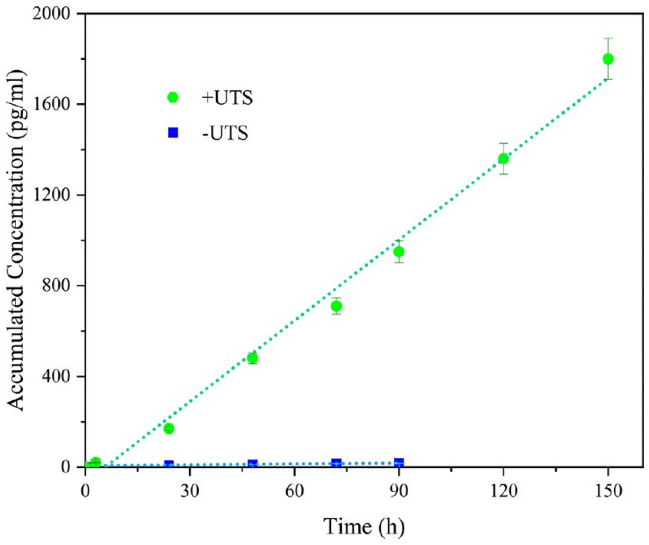

Figure 5. Accumulated concentration release of MSs with ultrasound and without ultrasound irradiation at pH 7.4 and T = 37 °C.

concentration of the MSs. The bFGF-MSs displayed higher cell viability percent potency after 48 h compared with 24 h incubation. The cell viability percent of bFGF-MSs without sonication was obtained at about 89% at 200 μg/mL (Figure 6b) after 24 h of incubation.

3.5. *In Vitro* Targeting Efficiency Study. For *in vitro* targeting, the activated human platelets were attached with FITC-bFGF MSs, followed by analysis with fluorescence microscopy and field emission scanning electron microscopy (FESEM). The presence of activated human platelet was first investigated by a fluorescence microscope. According to the microscopic cell morphology, the fluorescence images (Figure 7a) demonstrated that FITC-bFGF MSs and FITC-bFGF-platelet MSs efficiently surrounded the HUVECs. In the targeted group, visualization by fluorescence imaging displayed the presence of the platelet. The fluorescence intensity also indicated that, after 3 h of incubation, the intensity of platelet-MSs was maximized with + UTS. These results confirmed the targeting ability of the synthesized platelet-MSs.

Also, HUVECs incubated with bFGF-platelet MSs (Figure 7b,c) were directly observed by FESEM images. As seen in the images, platelet-MSs was incubated for 3 h with HUVECs (Figure 7b), and FITC-bFGF-platelet MSs was placed into the HUVEC (Figure 7c). The FESEM images exhibited the morphology with the smooth surface and discoid shape of the platelet in the cells.[64]

3.6. Cellular Uptake of MSs and MBs *In Vitro* Conditions. The cellular uptake of bFGF-free, bFGF-MSs, and bFGF-platelet-MSs by HUVECs *in vitro* conditions was evaluated by green fluorescence, and the images are displayed in Figure 8A. In the cells treated with free bFGF, a very weak signal was observed. In addition, a weak fluorescent signal was

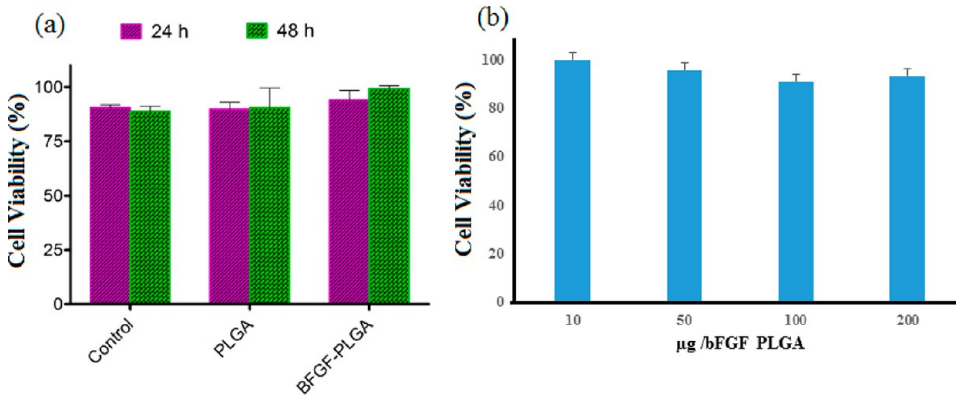

Figure 6. Cell viability study of bFGF- MSs (10, 50, 100, 200 μM) for 24 (a) and 48 h (b) against HUVECs.

https://doi.org/10.1021/acsomega.3c00067
ACS Omega 2023, 8, 11335−11350

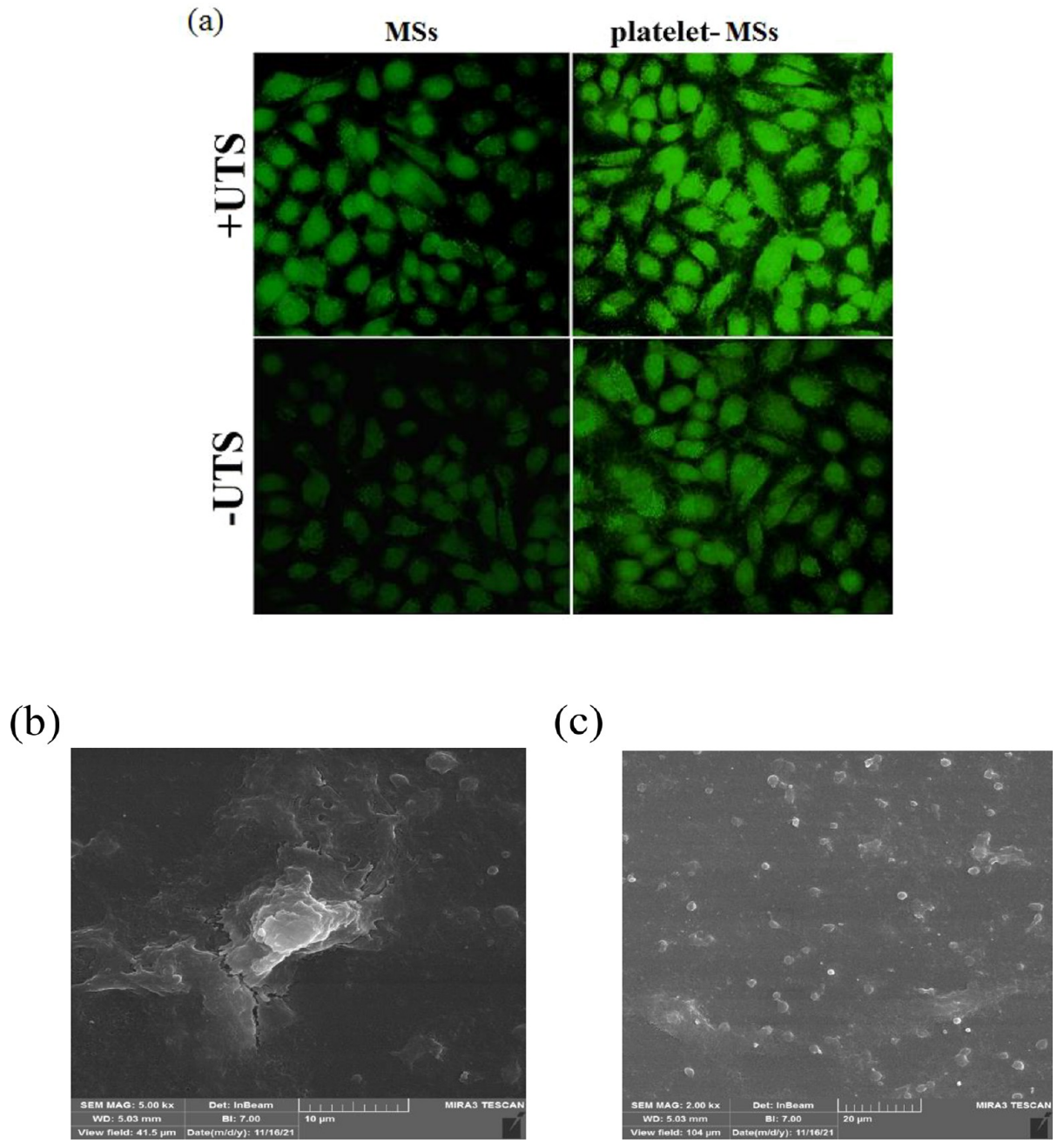

Figure 7. *In vitro* targeting efficiency of fluorescence intensity of HUVECs incubated with FITC-bFGF-MSs and FITC-bFGF-platelet MSs (with and without UTS) (a); FESEM images of HUVECs incubated with FITC-bFGF-MSs for 3 h (b) and discoid shape of the FITC-bFGF-platelet MSs placed into the cell (c).

detected in bFGF-MSs and bFGF-platelet-MSs in the −UTS group, but a strong signal was observed in the presence of UTS (+UTS) from the MBs and tested cells. These results confirmed the poor permeability of bFGF without MB as the carrier.

In bFGF-platelet-MSs, in the presence of + UTS compared to bFGF-MSs, the signals significantly increased (Figure 8B,C). Mean fluorescence intensity (MFI) data of the control, bFGF, bFGF-MSs, and bFGF-platelet-MSs groups were measured to confirm cell uptake value; the results are tabulated in Table 1.

From flow cytometry analysis, the HUVECs treated with bFGF in the presence of UTS (+UTS) exhibited no shifts compared to the control group (Figure 8B,C). Significantly stronger shifts were observed in the cells treated with bFGF-MSs and bFGF-platelet-MSs, instead of bFGF (Figure 8B,C). The flow cytometry analysis demonstrated that in the presence of UTS the bFGF uptake in bFGF-MSs and bFGF-platelet-MSs increased and, similar to the fluorescence images, the flow cytometry analysis confirmed that the use of UTS could further increase the bFGF cell uptake in bFGF-MSs and bFGF-platelet-MSs (panels c and d in Figure 8B,C). The uptake efficiency of the bFGF-platelet-MSs increased from less than 5% (−UTS) to nearly 24% (+UTS), indicating approximately a 5-fold improvement.

The targeting specificity of bFGF-platelet-MSs for platelet receptors was visually studied and compared with the cellular uptakes of bFGF-MSs on platelet receptor cells and by a

https://doi.org/10.1021/acsomega.3c00067
ACS Omega 2023, 8, 11335−11350

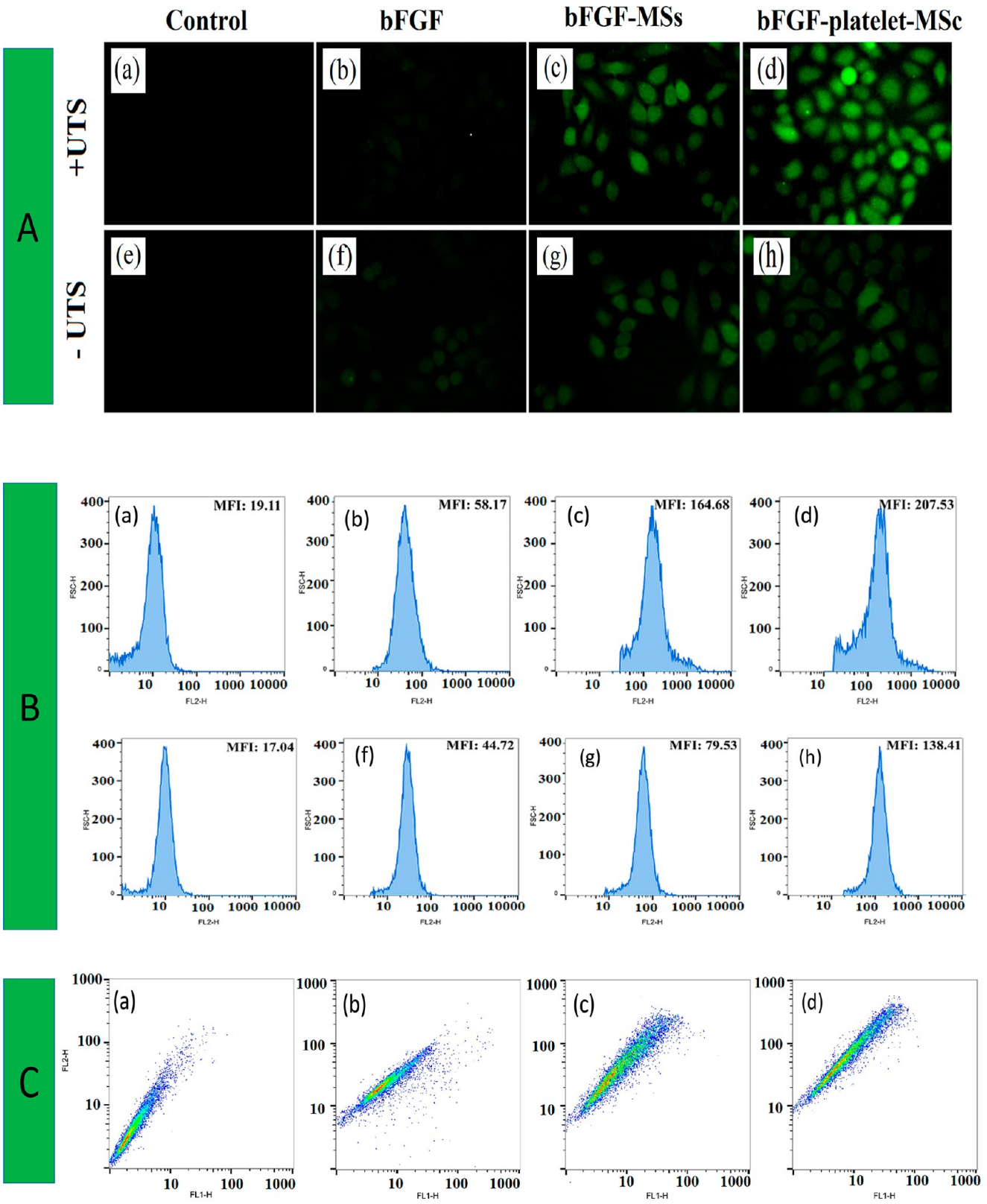

Figure 8. Fluorescence microscopy (A), cell uptake (B), and flow cytometry (C) results of HUVECs treated with FITC exhibiting bFGF cellular uptake *in vitro* conditions. (a) Control (+UTS), (b) bFGF (+UTS), (c) bFGF-MSs (+UTS), (d) bFGF-platelet-MSs (+UTS), (e) control (−UTS), (f) bFGF (−UTS), (g) bFGF-MSs (−UTS), and (h) bFGF-platelet-MSs (−UTSl).

fluorescence microscope [Figure 8A(a−h)]. The green fluorescent ring around the bGFGF-MBs [Figure 8A(c)] and bFGF-platelet-MSs [Figure 8 A(d)] indicated that the platelet was successfully attached to the surface of the MBs. Slight green fluorescence can be detected in the cells incubated with no targeted MSs. The cellular uptake of bFGF-platelet-MSs

https://doi.org/10.1021/acsomega.3c00067
ACS Omega 2023, 8, 11335−11350

Table 1. MFI Data of the Control, bFGF, bFGF-MSs, and bFGF-platelet-MSs Samples

	Control	bFGF	bFGF-MSs	bFGF-platelet-MSs
MFI (−UTS)	17.04	44.72	79.53	138.41
MFI (+UTS)	19.11	58.17	164.68	207.53

was considerably higher than that of bFGF-MSs in HUVECs, demonstrating that platelet-MSs facilitated the bFGF uptake, which is known as the targeted delivery. As a result, enhanced bFGF fluorescence intensity, attributed to the platelets receptor-mediated endocytosis of MSs, indicated the adequate performance of platelet in internalizing the MSs into the cells by a specific targeting mechanism.

The MB-based systems were able to deliver a sufficient quantity of bFGF to the MI tissues. In addition, the MBs considerably developed the cell uptake of the labeled bFGF-MBs into HUVECs compared to free bFGF (panels c and d in Figure 8B,C). It was shown that the efficiency of bFGF-MSs delivery would be essentially increased with UTS to a more optimal rate. Therefore, UTS was applied for this objective that as a noninvasive technique has previously demonstrated some success in developing protein delivery to the heart.[65] Zhao et al.[66] reported that bFGF-loaded microbubbles with ultrasound-targeted microbubble destruction (UTMD) exhibited promise as a molecular therapy for the heart of diabetic rats. However, in the traditional MBs with gas−core, the drug loading space is limited, and the acoustic resonance can influence the loaded drugs on the surface of MBs and reduce ultrasonic image resolution as well as the protein loading on the MBs.[67]

3.7. *In Vivo* Targeting. Targeting a specific location is a vital stage to obtaining the desired effects, which could be applied to improve residence time and payload delivery. The targeted MSs were collected in the ischemic myocardium region due to the enhanced permeability and retention (EPR) effect.[68] The results demonstrated that fluorescent detection in the targeted group displayed that the signal at the damaged heart site gradually increased (Figure 9a). Conversely, significant fluorescence was not seen in the nontargeted group at the damaged heart site (Figure 9b). Our results indicated that platelet conjugation with ultrasound-targeted microbubbles increases the bFGF delivery during ischemic compared with nontargeted MSs. Li et al.[69] reported platelet membrane biomimetic magnetic nanocarriers for targeted delivery and their role in targeting adhesion to the damaged blood vessel during ischemic stroke. Their results indicated that the fluorescence signal increased after 24 h. This targeted treatment increased the cellular uptake and endocytosis of MSs and therefore caused the adequate performance of platelet in internalizing the microspheres into the cells by a specific targeting mechanism.

4. CONCLUSIONS

We developed an injectable targeted PFH microbubble incorporated with bFGF as an adaptable platform for MI therapy. The PLGA with an uncapped free carboxylic acid at one end was used in this study. The carboxylic acids were activated via EDC/NHS chemistry to conjugate amine groups. PLGA-*g*-heparin was prepared by conjugating EDA to the PLGA backbone, followed by a reaction with heparin via EDC/NHS chemistry. PLGA-HP-PEG-cRGD-platelet MSs were prepared using a microfluidic device, in which PFH constituted the core and PLGA-HP-PEG-cRGD-platelet and gold nanoparticles were placed in the shell. These MSs were triggered by heat and US. Based on the unique ADV effect of PFH, these microspheres exhibited gas−liquid phase transition under ultrasound irradiation. The biocompatible MSs demonstrated an ultrasound-responsive feature for contrast ultrasound imaging. The MSs exhibited efficient bFGF encapsulation, and their potentiality for the controlled release of bFGF could be improved using focused ultrasound. The bFGF-platelet MBs significantly enhanced the efficiency of bFGF, cellular uptake, and flow cytometry without obvious cytotoxicity. As a result, enhanced bFGF fluorescence intensity, which was attributed to the platelets receptor-mediated endocytosis of MSs, indicated the effective performance of platelet in internalizing the MSs into the cells by a specific targeting mechanism. Furthermore, *in vitro* and *in vivo* targeting experiments showed that the platelet was successfully attached to the shell.

Our results showed that the MB formation using the UTS technique was an acceptable strategy to deliver bFGF by targeting, and bFGF delivery could notably increase by UTS in the MI tissue.

■ ASSOCIATED CONTENT

Supporting Information

The Supporting Information is available free of charge at https://pubs.acs.org/doi/10.1021/acsomega.3c00067.

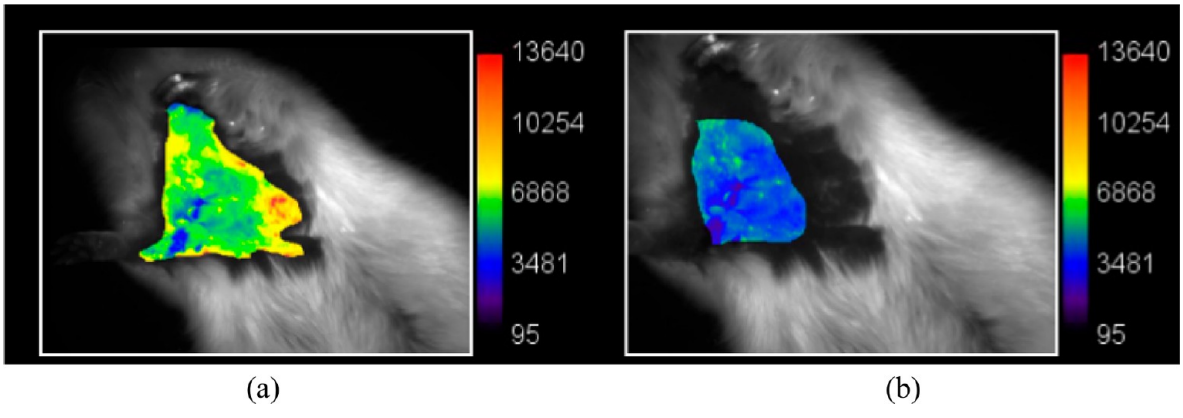

Figure 9. *In vivo* targeting images of FITC-platelet MSs (a) and FITC-MSs (b) by using fluorescence assessments.

https://doi.org/10.1021/acsomega.3c00067
ACS Omega 2023, 8, 11335−11350

FTIR spectra and ^{1}HNMR spectra of compounds (PDF)

AUTHOR INFORMATION

Corresponding Author

Farhang Abbasi − *Institute of Polymeric Materials and Faculty of Polymer Engineering, Sahand University of Technology, Tabriz 5331817634, Iran;* orcid.org/0000-0001-9770-4255; Email: f.abbasi@sut.ac.ir

Authors

Aliyeh Ghamkhari − *Institute of Polymeric Materials and Faculty of Polymer Engineering, Sahand University of Technology, Tabriz 5331817634, Iran*

Hossein Ahmadi Tafti − *Research Center for Advanced Technologies in Cardiovascular Medicine, Tehran Heart Center, Tehran University of Medical Sciences, Tehran 1416753955, Iran*

Shahram Rabbani − *Research Center for Advanced Technologies in Cardiovascular Medicine, Tehran Heart Center, Tehran University of Medical Sciences, Tehran 1416753955, Iran*

Marjan Ghorbani − *Nutrition Research Center, Tabriz University of Medical Sciences, Tabriz IR 51656-65811, Iran*

Mohammad Adel Ghiass − *Tissue Engineering Department, Tarbiat Modares University, Tehran 1411713116, Iran*

Fariborz Akbarzadeh − *Cardiovascular Research Center, Tabriz University of Medical Sciences, Tabriz 5166/15731, Iran*

Complete contact information is available at: https://pubs.acs.org/10.1021/acsomega.3c00067

Notes

The authors declare no competing financial interest.

ACKNOWLEDGMENTS

This work has been partially supported by the Iran National Science Foundation (INSF) under Project No. 96010402. Some figures (in Graphical Abstract, Scheme 1, and Scheme 2) were created with https://BioRender.com.

REFERENCES

(1) Wu, Y.; Chang, T.; Chen, W.; Wang, X.; Li, J.; Chen, Y.; Yu, Y.; Shen, Z.; Yu, Q.; Zhang, Y. Release of VEGF and BMP9 from Injectable Alginate Based Composite Hydrogel for Treatment of Myocardial Infarction. *Bioact. Mater.* **2021**, *6*, 520−528.

(2) Timmis, A.; Townsend, N.; Gale, C. P.; Torbica, A.; Lettino, M.; Petersen, S. E.; Mossialos, E. A.; Maggioni, A. P.; Kazakiewicz, D.; May, H. T.; De Smedt, D. European Society of Cardiology: Cardiovascular Disease Statistics 2019. *Europ. Heart J.* **2020**, *41*, 12−85.

(3) Xu, C.; Xu, L.; Ohorodnyk, P.; Roth, M.; Chen, B.; Li, S. Contrast Agent-free Synthesis and Segmentation of Ischemic Heart Disease Images Using Progressive Sequential Causal GANs. *Med. Image Anal.* **2020**, *62*, 101668.

(4) Yao, X.; Teh, B. M.; Li, H.; Hu, Y.; Huang, J.; Lv, C.; Bu, S.; Zheng, M.; Shen, Y. Acellular Collagen Scaffold with Basic Fibroblast Growth Factor for Repair of Traumatic Tympanic Membrane Perforation in a Rat Model. Otolaryngol. *Head Neck Surg.* **2021**, *164*, 381−390.

(5) Li, Z.; Zhu, D.; Hui, Q.; Bi, J.; Yu, B.; Huang, Z.; Hu, S.; Wang, Z.; Caranasos, T.; Rossi, J.; Li, X. Injection of ROS-responsive hydrogel loaded with basic fibroblast growth factor into the pericardial cavity for heart repair. *Adv. Funct. Mater.* **2021**, *31*, 2004377.

(6) Yin, X. X.; Zheng, X. R.; Peng, W.; Wu, M. L.; Mao, X. Y. Vascular endothelial growth factor (VEGF) as a vital target for brain inflammation during the COVID-19 outbreak. *ACS Chem. Neurosci.* **2020**, *11*, 1704−1705.

(7) Romdhane, K.; Zola, M.; Matet, A.; Daruich, A.; Elalouf, M.; Behar-Cohen, F.; Mantel, L. Predictors of treatment response to intravitreal anti-vascular endothelial growth factor (anti-VEGF) therapy for choroidal neovascularisation secondary to chronic central serous chorioretinopathy. *Br J. Ophthalmol.* **2020**, *104*, 910−916.

(8) Quartuccio, L.; Fabris, M.; Sonaglia, A.; Peghin, M.; Domenis, R.; Cifù, A.; Curcio, F.; Tascini, C. Interleukin 6, soluble interleukin 2 receptor alpha (CD25), monocyte colony-stimulating factor, and hepatocyte growth factor linked with systemic hyperinflammation, innate immunity hyperactivation, and organ damage in COVID-19 pneumonia. *Cytokine* **2021**, *140*, 155438.

(9) Villanueva, S.; Contreras, F.; Tapia, A. Basic fibroblast growth factor reduces functional and structural damage in chronic kidney disease. *Am. J. Physiol Renal Physiol.* **2014**, *306*, 430−441.

(10) Tan, X. H.; Zheng, X. M.; Yu, L. X.; He, J.; Zhu, H. M.; Ge, X. P.; Ren, X. L.; Ye, F. Q.; Bellusci, S.; Xiao, J.; Li, X. K. Fibroblast growth factor 2 protects against renal ischaemia/reperfusion injury by attenuating mitochondrial damage and proinflammatory signalling. *J. Cell Mol. Med.* **2017**, *21*, 2909−2925.

(11) Lin, X.; Zhao, L.; Tang, S.; Zhou, Q.; Lin, Q.; Li, X.; Zheng, H.; Gao, H. Metabolic effects of basic fibroblast growth factor in streptozotocin-induced diabetic rats: a (1) HNMR-based metabolomics investigation. *Sci. Rep.* **2016**, *6*, 36474.

(12) Cho, Y.; Baek, J.; Lee, E.; Im, S. G. Heparin-mediated electrostatic immobilization of bFGF via functional polymer films for enhanced self-renewal of human neural stem cells. *J. Mater.Chem. B* **2021**, *9*, 2084−2091.

(13) Sheng, W. S.; Xu, H. L.; Zheng, L.; Zhuang, Y. D.; Jiao, L. Z.; Zhou, J. F.; ZhuGe, D. L.; Chi, T. T.; Zhao, Y. Z.; Lan, L. Intrarenal delivery of bFGF-loaded liposome under guiding of ultrasound-targeted microbubble destruction prevent diabetic nephropathy through inhibition of inflammation. Artif. Cells. *Nanomed. Biotechnol.* **2018**, *46*, 373−385.

(14) Fan, Z.; Xu, Z.; Niu, H.; Sui, Y.; Li, H.; Ma, J.; Guan, J. Spatiotemporal delivery of basic fibroblast growth factor to directly and simultaneously attenuate cardiac fibrosis and promote cardiac tissue vascularization following myocardial infarction. *J. Controlled Release* **2019**, *311*, 233−244.

(15) Ikegami, Y.; Ijima, H. Development of heparin-conjugated nanofibers and a novel biological signal by immobilized growth factors for peripheral nerve regeneration. *J. Biosci. Bioeng.* **2020**, *129*, 354−362.

(16) Jain, A.; Tiwari, A.; Verma, A.; Jain, S. K. Ultrasound-based triggered drug delivery to tumors. *Drug Delivery Transl. Res.* **2018**, *8*, 150−164.

(17) Wang, X.; Yan, F.; Liu, X.; Wang, P.; Shao, S.; Sun, Y.; Sheng, Z.; Liu, Q.; Lovell, J. F.; Zheng, H. Enhanced drug delivery using sonoactivatable liposomes with membrane-embedded porphyrins. *J. Controlled Release* **2018**, *286*, 358−368.

(18) Izadifar, Z.; Babyn, P.; Chapman, D. Ultrasound cavitation/microbubble detection and medical applications. *J. Med. Biol. Eng.* **2019**, *39*, 259−276.

(19) Kooiman, K.; Roovers, S.; Langeveld, S. A.; Kleven, R. T.; Dewitte, H.; O'Reilly, M. A.; Escoffre, J. M.; Bouakaz, A.; Verweij, M. D.; Hynynen, K.; Lentacker, I. Ultrasound-responsive cavitation nuclei for therapy and drug delivery. *Ultrasound med. Boil.* **2020**, *46*, 1296−1325.

(20) Wang, S.; Hossack, J. A.; Klibanov, A. L. Targeting of microbubbles: contrast agents for ultrasound molecular imaging. *J. Drug Target.* **2018**, *26*, 420−434.

(21) Liu, Y.; Gong, Y.; Xie, W.; Huang, A.; Yuan, X.; Zhou, H.; Zhu, X.; Chen, X.; Liu, J.; Liu, J.; Qin, X. Microbubbles in combination with focused ultrasound for the delivery of quercetin-modified sulfur

nanoparticles through the blood brain barrier into the brain parenchyma and relief of endoplasmic reticulum stress to treat Alzheimer's disease. *Nanoscale* **2020**, *12*, 6498−6511.
(22) Du, M.; Chen, Y.; Tu, J.; Liufu, C.; Yu, J.; Yuan, Z.; Gong, X.; Chen, Z. Ultrasound Responsive Magnetic Mesoporous Silica Nanoparticle-Loaded Microbubbles for Efficient Gene Delivery. *ACS Biomater. Sci. Eng.* **2020**, *6*, 2904−2912.
(23) Teraphongphom, N.; Chhour, P.; Eisenbrey, J. R.; Naha, P. C.; Witschey, W. R.; Opasanont, B.; Jablonowski, L.; Cormode, D. P.; Wheatley, M. A. Nanoparticle loaded polymeric microbubbles as contrast agents for multimodal imaging. *Langmuir* **2015**, *31*, 11858−11867.
(24) Al-Jawadi, S.; Thakur, S. S. Ultrasound-responsive lipid microbubbles for drug delivery: A review of preparation techniques to optimize formulation size, stability and drug loading. *Int. J. Pharm.* **2020**, *585*, 119559.
(25) Aneja, P.; Rahman, M.; Beg, S.; Aneja, S.; Dhingra, V.; Chugh, R. Cancer targeted magic bullets for effective treatment of cancer. *Recent pat. anti-infective drug discov.* **2015**, *9*, 121−135.
(26) Khan, A. H.; Jiang, X.; Surwase, S.; Gultekinoglu, M.; Bayram, C.; Sathisaran, I.; Bhatia, D.; Ahmed, J.; Wu, B.; Ulubayram, K.; Edirisinghe, M. Effectiveness of oil-layered albumin microbubbles produced using microfluidic T-junctions in series for in vitro inhibition of tumor cells. *Langmuir* **2020**, *36*, 11429−11441.
(27) Wang, Q.; Xue, C.; Qin, Y.; Zhang, X.; Li, Y. The fabrication of protein microbubbles with diverse gas core and the novel exploration on the role of interface introduction in protein crystallization. *Colloids Surf. A Physicochem. Eng. Asp.* **2020**, *589*, 124471.
(28) Zhu, J. X.; Zhu, W. T.; Hu, J. H.; Yang, W.; Liu, P.; Liu, Q. H.; Bai, Y. X.; Xie, R. Curcumin-loaded poly (L-lactide-co-glycolide) microbubble-mediated Sono-photodynamic therapy in liver cancer cells. *Ultrasound Med. Biol.* **2020**, *46*, 2030−2043.
(29) Shen, X.; Li, T.; Xie, X.; Feng, Y.; Chen, Z.; Yang, H.; Wu, C.; Deng, S.; Liu, Y. PLGA-based drug delivery systems for remotely triggered cancer therapeutic and diagnostic applications. *Bioeng. Biotechnol.* **2020**, *8*, 381.
(30) Josefsson, L.; Goodall, D.; Emmer, A. A. Implementation of a ultraviolet area imaging detector for analysis of polyvinyl alcohol microbubbles by capillary electrophoresis. *J. Chromatogr. A* **2020**, *1619*, 460899.
(31) Wang, Y.; Sun, W.; Ding, L.; Liu, W.; Tian, L.; Zhao, Y.; Zhang, M.; Wang, X. A study on the feasibility and mechanism of enhanced co-coagulation dissolved air flotation with chitosan-modified microbubbles. *J. Water Process. Eng.* **2021**, *40*, 101847.
(32) Zuo, Q.; Guo, R.; Liu, Q.; Hong, A.; Shi, Y.; Kong, Q.; Huang, Y.; He, L.; Xue, W. Heparin-conjugated alginate multilayered microspheres for controlled release of bFGF. *Biomed. Mater.* **2015**, *10*, No. 035008.
(33) Mohamedi, G.; Azmin, M.; Pastoriza-Santos, I.; Huang, V.; Pérez-Juste, J.; Liz-Marzán, L. M.; Edirisinghe, M.; Stride, E. Effects of gold nanoparticles on the stability of microbubbles. *Langmuir* **2012**, *28*, 13808−13815.
(34) Zhong, Q.; Yoon, B. C.; Aryal, M.; Wang, J. B.; Ilovitsh, T.; Baikoghli, M. A.; Hosseini-Nassab, N.; Karthik, A.; Cheng, R. H.; Ferrara, K. W.; Airan, R. D. Polymeric perfluorocarbon nanoemulsions are ultrasound-activated wireless drug infusion catheters. *Biomaterials* **2019**, *206*, 73−86.
(35) Duarte, A. R. C.; Ünal, B.; Mano, J. F.; Reis, R. L.; Jensen, K. F. Microfluidic production of perfluorocarbon-alginate core−shell microparticles for ultrasound therapeutic applications. *Langmuir* **2014**, *30*, 12391−12399.
(36) Baghbani, F.; Chegeni, M.; Moztarzadeh, F.; Hadian-Ghazvini, S.; Raz, M. Novel ultrasound-responsive chitosan/perfluorohexane nanodroplets for image-guided smart delivery of an anticancer agent: Curcumin. *Mater. Sci. Eng. C* **2017**, *74*, 186−193.
(37) Xu, J.; Zhou, J.; Zhong, Y.; Zhang, Y.; Liu, J.; Chen, Y.; Deng, L.; Sheng, D.; Wang, Z.; Ran, H.; Guo, D. Phase transition nanoparticles as multimodality contrast agents for the detection of thrombi and for targeting thrombolysis: in vitro and in vivo experiments. *ACS Appl. Mater. Interfaces.* **2017**, *9*, 42525−42535.
(38) Zhong, Y.; Zhang, Y.; Xu, J.; Zhou, J.; Liu, J.; Ye, M.; Zhang, L.; Qiao, B.; Wang, Z. G.; Ran, H. T.; Guo, D. Low-intensity focused ultrasound-responsive phase-transitional nanoparticles for thrombolysis without vascular damage: a synergistic nonpharmaceutical strategy. *ACS Nano* **2019**, *13*, 3387−3403.
(39) Fernandes, D. A.; Fernandes, D. D.; Li, Y.; Wang, Y.; Zhang, Z.; Rousseau, D.; Gradinaru, C. C.; Kolios, M. C. Synthesis of stable multifunctional perfluorocarbon nanoemulsions for cancer therapy and imaging. *Langmuir* **2016**, *32*, 10870−10880.
(40) Bai, S.; Liao, J.; Zhang, B.; Zhao, M.; You, B.; Li, P.; Ran, H.; Wang, Z.; Shi, R.; Zhang, G. Multimodal and multifunctional nanoparticles with platelet targeting ability and phase transition efficiency for the molecular imaging and thrombolysis of coronary microthrombi. *Biomat. Sci.* **2020**, *8*, 5047−5060.
(41) Ye, M.; Zhou, J.; Zhong, Y.; Xu, J.; Hou, J.; Wang, X.; Wang, Z.; Guo, D. SR-A-targeted phase-transition nanoparticles for the detection and treatment of atherosclerotic vulnerable plaques. *ACS Appl. Mater. Interfaces.* **2019**, *11*, 9702−9715.
(42) Chen, X.; Zhang, Y.; Zhang, H.; Zhang, L.; Liu, L.; Cao, Y.; Ran, H.; Tian, J. A non-invasive nanoparticles for multimodal imaging of ischemic myocardium in rats. *J. nanobiotech.* **2021**, *19*, 1−18.
(43) Chen, C.; Wang, Y.; Tang, Y.; Wang, L.; Jiang, F.; Luo, Y.; Gao, X.; Li, P.; Zou, J. Bifidobacterium-mediated high-intensity focused ultrasound for solid tumor therapy: comparison of two nanoparticle delivery methods. *Int. J. Hyperth.* **2020**, *37*, 870−878.
(44) Cruz, M. A.; Bohinc, D.; Andraska, E. A.; Alvikas, J.; Raghunathan, S.; Masters, N. A.; van Kleef, N. D.; Bane, K. L.; Hart, K.; Medrow, K.; Sun, M. Nanomedicine platform for targeting activated neutrophils and neutrophil−platelet complexes using an α1-antitrypsin-derived peptide motif. *Nature Nanotechnology.* **2022**, *17*, 1004−14.
(45) Schneider, D. J.; McMahon, S. R.; Ehle, G. L.; Chava, S.; Taatjes-Sommer, H. S.; Meagher, S. Assessment of Cardiovascular Risk by the Combination of Clinical Risk Scores Plus Platelet Expression of FcγRIIa. *Am. J. Cardiol.* **2020**, *125*, 670−672.
(46) Günther, F.; Heidt, T.; Kramer, M.; Khanicheh, E.; Klibanov, A. L.; Geibel-Zehender, A.; Ferrante, E. A.; Hilgendorf, I.; Wolf, D.; Zirlik, A.; Reinöhl, J. Dual targeting improves capture of ultrasound microbubbles towards activated platelets but yields no additional benefit for imaging of arterial thrombosis. *Sci. Rep.* **2017**, *7*, 1−8.
(47) Chen, Z.; Koenig, S. C.; Slaughter, M. S.; Griffith, B. P.; Wu, Z. J. Quantitative characterization of shear-induced platelet receptor shedding: glycoprotein Ibα, glycoprotein VI and glycoprotein IIb/IIIa. *J. A.S.A.I.O.* **2018**, *64*, 773.
(48) Hu, G.; Liu, C.; Liao, Y.; Yang, L.; Huang, R.; Wu, J.; Xie, J.; Bundhoo, K.; Liu, Y.; Bin, J. Ultrasound molecular imaging of arterial thrombi with novel microbubbles modified by cyclic RGD in vitro and in vivo. *Thrombosis and haemostasis.* **2012**, *107*, 172−183.
(49) Zhang, C.; Shang, Y.; Chen, X.; Midgley, A. C.; Wang, Z.; Zhu, D.; Wu, J.; Chen, P.; Wu, L.; Wang, X.; Zhang, K. Supramolecular Nanofibers Containing Arginine-Glycine-Aspartate (RGD) Peptides Boost Therapeutic Efficacy of Extracellular Vesicles in Kidney Repair. *ACS Nano* **2020**, *14*, 12133−12147.
(50) Lee, I.; Marchant, R. E. Dynamic Debonding Force Measurements of Ligand (RGD)-Platelet Receptor (GP IIb/IIIa) System under Physiological Conditions. *Microsc. Microanal.* **2000**, *6*, 974−975.
(51) Sanna, V.; Pintus, G.; Bandiera, P.; Anedda, R.; Punzoni, S.; Sanna, B.; Migaleddu, V.; Uzzau, S.; Sechi, M. Development of polymeric microbubbles targeted to prostate-specific membrane antigen as prototype of novel ultrasound contrast agents. *Mol. Pharmaceutics* **2011**, *8*, 748−57.
(52) Wang, Q.; He, Y.; Zhao, Y.; Xie, H.; Lin, Q.; He, Z.; Wang, X.; Li, J.; Zhang, H.; Wang, C.; Gong, F. A thermosensitive heparin-poloxamer hydrogel bridges aFGF to treat spinal cord injury. *ACS Appl. Mater. Interfaces.* **2017**, *9*, 6725−45.

https://doi.org/10.1021/acsomega.3c00067
ACS Omega 2023, 8, 11335−11350

(53) Zhao, Y. Z.; Tian, X. Q.; Zhang, M.; Cai, L.; Ru, A.; Shen, X. T.; Jiang, X.; Jin, R. P.; Zheng, L.; Hawkins, K.; Charkrabarti, S. Functional and pathological improvements of the hearts in diabetes model by the combined therapy of bFGF-loaded nanoparticles with ultrasound-targeted microbubble destruction. *J. Controlled Release* **2014**, *186*, 22−31.
(54) Loureiro, J. A.; Gomes, B.; Fricker, G.; Coelho, M. A.; Rocha, S.; Pereira, M. C. Cellular uptake of PLGA nanoparticles targeted with anti-amyloid and anti-transferrin receptor antibodies for Alzheimer's disease treatment. *Colloids and Surf. B: Biointerfaces.* **2016**, *145*, 8−13.
(55) Liu, J.; Xu, J.; Zhou, J.; Zhang, Y.; Guo, D.; Wang, Z. Fe_3O_4-based PLGA nanoparticles as MR contrast agents for the detection of thrombosis. *Int. J. Nanomedicine.* **2017**, *12*, 1113.
(56) Tian, J. L.; Zhao, Y. Z.; Jin, Z.; Lu, C. T.; Tang, Q. Q.; Xiang, Q.; Sun, C. Z.; Zhang, L.; Xu, Y. Y.; Gao, H. S.; Zhou, Z. C. Synthesis and characterization of Poloxamer 188-grafted heparin copolymer. *Drug. Dev. Ind. Pharm.* **2010**, *36*, 832−838.
(57) Esther, J.; Sridevi, V. Synthesis and characterization of chitosan-stabilized gold nanoparticles through a facile and green approach. *Gold Bulletin* **2017**, *50*, 1−5.
(58) Salem, D. S.; Sliem, M. A.; El-Sesy, M.; Shouman, S. A.; Badr, Y. Improved chemo-photothermal therapy of hepatocellular carcinoma using chitosan-coated gold nanoparticles. *J. Photochem. Photobiol., B* **2018**, *182*, 92−99.
(59) Ojea-Jiménez, I.; Bastús, N. G.; Puntes, V. Influence of the sequence of the reagents addition in the citrate-mediated synthesis of gold nanoparticles. *J. Phys. Chem. C* **2011**, *115*, 15752−15757.
(60) Shanei, A.; Shanei, M. M. Effect of gold nanoparticle size on acoustic cavitation using chemical dosimetry method. *Ultrason Sonochem.* **2017**, *34*, 45−50.
(61) Duncanson, W. J.; Arriaga, L. R.; Ung, W. L.; Kopechek, J. A.; Porter, T. M.; Weitz, D. A. Microfluidic Fabrication of Perfluorohexane-Shelled Double Emulsions for Controlled Loading and Acoustic-Triggered Release of Hydrophilic Agents. *Langmuir* **2014**, *30*, 13765−13770.
(62) Zhou, Y.; Wang, Z.; Chen, Y.; Shen, H.; Luo, Z.; Li, A.; Wang, Q.; Ran, H.; Li, P.; Song, W.; Yang, Z. Microbubbles from gas-generating perfluorohexane nanoemulsions for targeted temperature-sensitive ultrasonography and synergistic HIFU ablation of tumors. *Adv. Mater. Lett.* **2013**, *25*, 4123−4130.
(63) Wang, Y.; Sui, G.; Teng, D.; Wang, Q.; Qu, J.; Zhu, L.; Ran, H.; Wang, Z.; Jin, C.; Wang, H. Low intensity focused ultrasound (LIFU) triggered drug release from cetuximab-conjugated phase-changeable nanoparticles for precision theranostics against anaplastic thyroid carcinoma. *Biomat. Sci.* **2019**, *7*, 196−210.
(64) De Paoli Lacerda, S. H.; Semberova, J.; Holada, K.; Simakova, O.; Hudson, S. D.; Simak, J. Carbon nanotubes activate store-operated calcium entry in human blood platelets. *ACS Nano* **2011**, *5*, 5808−5813.
(65) Zhou, Q.; Deng, Q.; Hu, B.; Wang, Y. J.; Chen, J. L.; Cui, J. J.; Cao, S.; Song, H. N. Ultrasound combined with targeted cationic microbubble-mediated angiogenesis gene transfection improves ischemic heart function. *Exp. Ther. Med.* **2017**, *13*, 2293−2303.
(66) Zhao, Y. Z.; Tian, X. Q.; Zhang, M.; Cai, L.; Ru, A.; Shen, X. T.; Jiang, X.; Jin, R. P.; Zheng, L.; Hawkins, K.; Charkrabarti, S. Functional and pathological improvements of the hearts in diabetes model by the combined therapy of bFGF-loaded nanoparticles with ultrasound-targeted microbubble destruction. *J. Controlled Release* **2014**, *186*, 22−31.
(67) Bekeredjian, R.; Chen, S.; Grayburn, P. A.; Shohet, R. V. Augmentation of cardiac protein delivery using ultrasound targeted microbubble destruction. *Ultrasound med. Boil.* **2005**, *31*, 687−691.
(68) Lin, X.; Yao, C.; Wu, F.; Shen, L.; Feng, Y.; Wang, L. Targeting delivery of Radix Ophiopogonis polysaccharide to ischemic/reperfused rat myocardium by long-circulating macromolecular and liposomal carriers. *Int. J. Nanomedicine.* **2015**, *10*, 5729−37.
(69) Li, M.; Li, J.; Chen, J.; Liu, Y.; Cheng, X.; Yang, F.; Gu, N. Platelet membrane biomimetic magnetic nanocarriers for targeted delivery and in situ generation of nitric oxide in early ischemic stroke. *ACS Nano* **2020**, *14*, 2024−2035.

https://doi.org/10.1021/acsomega.3c00067
ACS Omega 2023, 8, 11335−11350